

THE GALEX-GAIA-EDR3 CATALOGUE OF SINGLE AND BINARY WHITE DWARFS

RYAN JACKIM¹, JEREMY HEYL¹, AND HARVEY RICHER¹

¹Department of Physics and Astronomy, University of British Columbia, Vancouver, B.C. V6T 1Z1, Canada
Version April 12, 2024

ABSTRACT

We present a catalogue of white dwarf candidates constructed from the GALEX and Gaia EDR3 catalogues. The catalogue contains 332,111 candidate binary white dwarf systems and 111,996 candidate single white dwarfs. Where available, the catalogue is augmented with photometry from Pan-STARRS DR1, SDSS DR12 and classifications from StarHorse. We fit photometric data with modeled white dwarf cooling sequences to derive mass, age and effective temperature of the white dwarf as well as mass estimates for the companion. We test our classifications against StarHorse, the Gentile-Fusillo Gaia EDR3 catalogue, and white-dwarf-main-sequence binaries identified in SDSS DR12. This catalogue provides a unique probe of the binarity of white dwarfs as well as the abundance of white-dwarf giant binaries and large mass-ratio stellar binaries which are difficult to probe otherwise.

Keywords: White Dwarf – Binaries: general – Catalogues

1. INTRODUCTION

White dwarfs (WD) are stellar remnants originating from stars with mass less than $8 M_{\odot}$ which have reached the end of their evolutionary track. White-dwarf-main-sequence (WDMS) binaries are stellar systems with a WD that has formed from the initial primary star and a main sequence (MS) star. Similarly, white-dwarf-giant (WDG) binaries are systems where a WD has formed from the initial primary star and the secondary is now a giant star. We will refer to both types of systems generically as white-dwarf-non-degenerate (WDND) binaries (in contrast with double-degenerate, DD, binaries). WDs have low luminosity in the optical. When paired with a MS star more massive than a G star, it is difficult to identify the WD in the system due to the comparatively high luminosity of the companion. WDND systems offer the ability to construct studies on comprehensive binary population synthesis as well as insights into pre-cataclysmic variables (Willems & Kolb 2004). The evolution of WDND systems is largely controlled by the separation between the two stars. Three-quarters of WDND systems have orbital periods wide enough that the progenitor of the WD evolved independently of the other star in the system. Typically these systems will have an orbital period longer than 400 days (Willems & Kolb 2004). The remaining twenty five percent are close enough to each other to exchange mass during their stellar evolution. In these close binary systems, the more massive companion evolves off the main sequence first and moves onto the red giant branch (RGB). The RGB's outer atmosphere envelops the lower mass companion star and transfers mass. This is referred to as the common envelope (CE) stage. The RGB star's envelope is eventually ejected and it evolves into a WD creating a WDND system (Ivanova et al. 2013).

The atmospheres of WDs are generally found as either hydrogen-rich (DA) or helium-rich (DB). The fraction of WDs with helium-rich atmospheres increases significantly when T_{eff} of the WD is below 10,000 K. The reason for this change is likely caused by convection mixing the upper hydrogen atmosphere with the more massive

helium envelope beneath. It is expected that this convection process will turn all hydrogen-rich atmosphere WDs into helium-rich atmosphere WDs (Bergeron et al. 1997).

There have been several previous surveys that have attempted to gather samples of the WDND systems. The Sloan Digital Sky Survey (SDSS) identified WDND binary systems from Radial Velocity (RV) measurements of optical spectra. Using this technique, just over 3,300 WDND binaries have been identified (Rebassa-Mansergas et al. 2016). SDSS was primarily developed to identify quasars and galaxies, leading to most of the WDND systems identified being the same colour as quasars. This creates a bias towards hot ($\gtrsim 10,000$ - $15,000$ K) WDs with M-dwarf spectral type (i M3-4) companions (Rebassa-Mansergas et al. 2016, 2013). A correction done by Rebassa-Mansergas et al. (2013) attempted to use photometric data to identify WDND systems with colder WDs. Of the 3,419 candidates selected, 71% of the sources were expected to have a cool ($\lesssim 10,000$ - $15,000$ K) WD and a M-dwarf secondary (\sim M2-3). A similar method was employed by the Large Sky Area Multi-Object Fiber Spectroscopic Telescope (LAMOST) Survey which has identified 876 WDND systems (Ren et al. 2018). These previous studies of WDND systems have only observed WDND systems with M-dwarf companions. A study done by Rebassa-Mansergas et al. (2021) reported 112 WDND binary systems within 100 pc, located in the gap between the WD and MS region in the visual CMD. Their study did not include WDND systems lying within the MS region where the MS star dominates the light of the WD. They were able to conclude that their identification only accounted for roughly 9% of WDND systems and that 91% of WDND binaries remain obscured in the MS region. Thus, it is imperative that we identify alternative methods for assessing WDND systems enhance our understanding of the evolution of binary systems.

To attempt to identify WDND systems, we used several photometric survey's that contain optical and UV data. Two primary catalogues were utilized. The Galaxy Evolutionary Explorer (GALEX) is a NASA explorer

mission designed to carry out a space-based UV sky survey. The GALEX survey allows for UV detections of objects as faint as 23rd magnitude (Martin et al. 2005). WDs with a temperature range of 30,000 K to less than 4,500 K will emit in the UV (Bergeron et al. 2019). This makes the GALEX survey an excellent tool in which to identify WD systems. Gaia Early Data Release 3 (EDR3) (Gaia Collaboration et al. 2021) is a catalogue containing 1.8 billion stars limited to objects brighter than 21st G-magnitude. It contains improved photometry relative to Gaia Data Release 2 and detailed distance measurements of objects through observation of their parallactic shift. Gaia EDR3 contains the same astrometric data as Gaia DR3; therefore, the third data release does not add additional data for the match. The combined use of both these catalogues allows us to detect WDs through GALEX and collect both photometric and distance information of the systems through Gaia EDR3.

Using WD stars identified in GALEX and Gaia EDR3, we constructed a catalogue containing a total of 444,107 candidate single and binary WDs. Of these, 111,996 candidates match to WD objects identified by Gentile Fusillo et al. (2021). The remaining 309,584 are candidate WDND systems where the GALEX UV photometry reports values similar to WD, but Gaia EDR3 reports values similar to MS or giant stars. This was accomplished by identifying all GALEX entries near the WD sequence in the UV and cross-matching them with Gaia EDR3 entries. We then attempted to gather stellar parameter estimates for both the WD and non-degenerate secondary by applying a two-star fitting algorithm based on the stellar isochrones of Bressan et al. (2012) and the WD cooling models of Bédard et al. (2020). We analyzed the resulting masses for all the stars in the system and reported our estimated masses in our catalogue. Mass estimates from the StarHorse MS catalogue (Anders et al. 2021) and Gentile Fusillo et al. (2021) WD catalogue were included to supplement our estimates.

2. CATALOGUE CONSTRUCTION

2.1. Data Selection

The procedure to select WDND systems is similar to the Gentile Fusillo et al. (2021) selection of WD systems in the Gaia EDR3 data set. We sought to expand our list of potential WDND identifications by including likely UV-WDs as one of the components in the binary system. To begin, we produced a cross-match between GALEX and Gaia EDR3 using Vizier. The purpose behind this cross-match was to identify stellar systems with UV excesses that resembled WD stars. If these systems had an excess similar to a WD, it is likely that there is a WD present. We then implemented a broad cut which defines an area of the colour-magnitude diagram (CMD) space where WDs or WDND systems are located. At this stage, the cross-match was focused on gathering a wide selection of potential objects with little consideration for contaminants:

ADQL 1: Photometric Cut

```
NUVmag-DM-0.6*(FUVmag-NUVmag) > 8 OR
NUVmag-DM-
2*(NUVmag-phot_bp_mean_mag) > 8 OR
phot_g_mean_mag-DM-3*bp_rp > 8
```

where DM is the distance modulus determined using the Gaia EDR3 parallax. Our selection focused on locating white-dwarf-like objects within one of three wavelength regions. These three regions are: the far-UV (FUV) and near-UV (NUV) defined exclusively by the GALEX dataset in the left plot of Figure 1, the near-UV from GALEX to the Gaia Bp filter described in the center plot of Figure 1, and the Gaia EDR3 visual magnitudes described by the Bp and Rp filters shown in the right plot of Figure 1. The black line in Figure 1 depicts a cut where everything below the line is considered a WD or a WDND. Everything above the line is excluded from our catalogue. If an object was below the black line in one of the wavelength regions, it was considered a WD or WDND regardless of whether it succeeded in the other two regions.

A large fraction of our collected data had unreliable astrometric or photometric data. We apply the quality cuts in ADQL 2 to our sample, which excluded non-WD contaminants and entries with poor photometry.

ADQL 2: Error Cut

```
parallax_over_error >= 4 AND
(astrometric_excess_noise_sig < 2 OR
astrometric_excess_noise < 1.5 OR
astrometric_params_solved < 32)
```

Because of the potential presence of a companion star contaminating the photometry of the WD, the quality cuts were generous enough to allow for this circumstance.

Two additional cross-matches were done to identify if the objects had data from SDSS DR12 or Pan-STARRS DR1. If the objects matched SDSS or Pan-STARRS entries, the data were included in the catalogue. Those that did not were left blank.

After quality cuts were applied, 444,107 possible WD systems remain. Figure 2 describes the distribution of these 444,107 objects in the Gaia EDR3 photometric filters. The blue region signifies objects that were similar to WDs in Gaia EDR3 and the red signifies those that did not look like WDs in Gaia EDR3, but were similar to WDs in other wavelengths. Upon inspection of Figure 2, it is clear that there is a large variety of objects identified as WD across the MS and the evolved branch. The total numerical distribution of objects that succeeded our three different WD cuts can be seen in the weighted Venn diagram of Figure 3. The magenta circle depicts objects that look like WDs only in the GALEX FUV-NUV filters and not WDs in the GALEX NUV-Gaia Bp or Gaia Bp-Rp filters. The yellow circle describes objects that look like WDs only in GALEX NUV-Gaia Bp and not WDs in the GALEX FUV-NUV or Gaia Bp-Rp filters. Finally, the cyan slice (2199 stars), defines the number of objects that were identified as a WD in only the Gaia filters and not WDs in the NUV-Bp or FUV-NUV filters. A majority of the objects in the cyan slice, did not contain FUV data or were objects that existed above the WD sequence in the Gaia filters. If one of the circles has been overlapped by another, then the object looks like a WD in two filters. The central section where all three circles overlap describes the number of objects that look like WDs in all three filters. The cyan Gaia EDR3 circle in Figure 3, including all overlapping sections, directly depicted the blue region in Figure 2, totaled 134,523 objects. The yellow, pink and magenta circles correspond

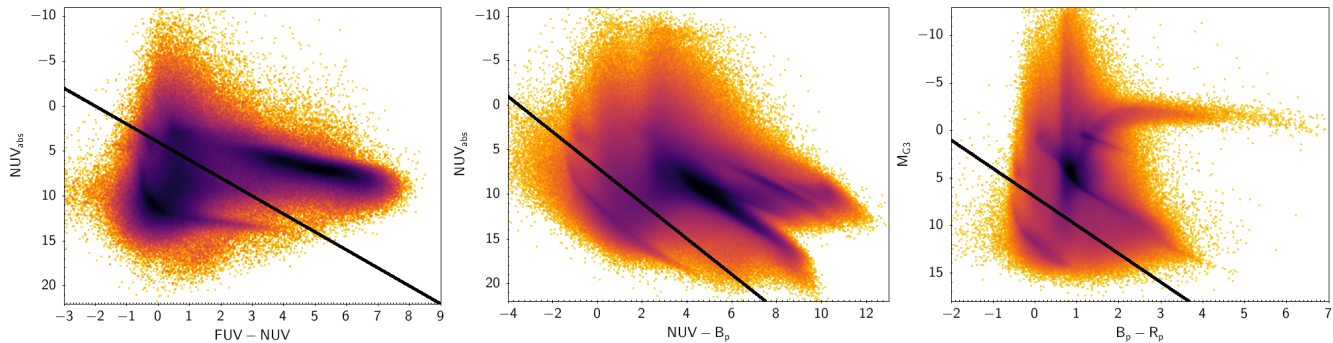


Figure 1. : The distribution of GALEX-Gaia EDR3 cross-match is shown in the above three figures. The left image depicts the objects that succeeded our cross-match in the GALEX FUV-NUV filters. The middle figure depicts the same objects in the GALEX NUV-Gaia Bp filters. The right figure depicts these objects in the Gaia Bp-Rp filters. The black line represents our cut described in ADQL 1. Objects that lie below the black line in any of these panels are considered WDs or WDND and included in our catalogue.

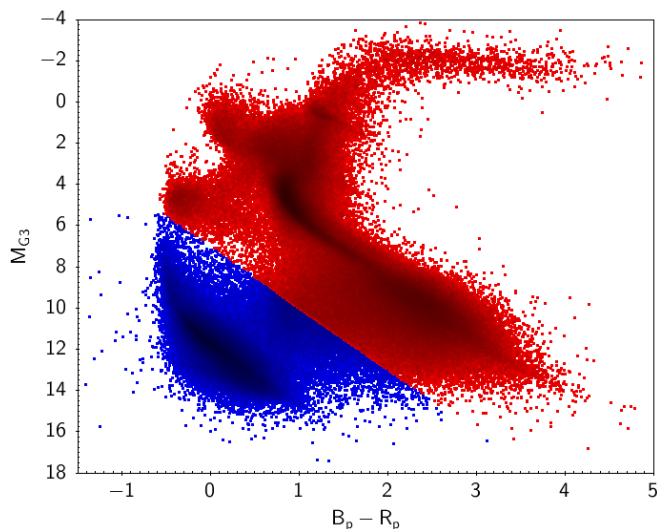


Figure 2. : Gaia absolute G magnitude and Bp-Rp of the 444,107 entries in the catalogue. The blue region represents objects that lie within or near the WD region in Gaia and the red region represents objects identified as a WD in the GALEX filters. The blue region contains 134,523 entries while the red region contains 309,584 entries.

to objects that were identified as WDs in GALEX UV but not Gaia optical bands and totaled 309,584 objects. The red region in Figure 2 corresponds to these 309,584 objects. By observing this red region in Figure 2, it is clear that there are many objects that appear to be MS or giant stars that look like WDs in the GALEX UV. Thus, we consider these 309,584 objects to be candidate WDND systems.

A number of entries in Figure 2 appear to lie within the WD sequence in the Gaia filters. To attempt to identify these possible single WDs, a cross-match was done with the Gentile Fusillo et al. (2021) WD catalogue. Of the 444,107 entries, 111,996 matched to WDs previously identified by Gentile Fusillo et al. (2021). A total of 332,111 objects remain unmatched.

2.2. Extinction

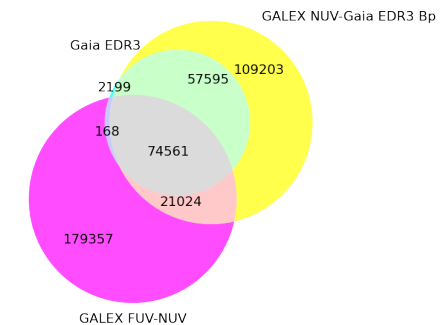


Figure 3. : This figure describes the number of entries in our catalogue that survived at least one of our cuts in the colour-magnitude diagram. The cyan slice (2,199 stars) indicates the number of objects that appear as WDs only in the Gaia CMD and not the GALEX NUV-Gaia Bp or GALEX FUV-NUV CMD. The yellow circle describes the number of objects only identified as WDs in GALEX NUV-Gaia Bp filters and not the Gaia Bp-Rp or GALEX FUV-NUV CMD. The magenta circle illustrates the number of objects only identified as WDs in the GALEX FUV-NUV filters and not the Gaia Bp-Rp or GALEX NUV-Gaia Bp CMD. The intersections of the circles indicate objects which have two or more WD identifications. The 168 objects identified as a WD only in Gaia EDR3 and GALEX FUV-NUV CMD and not in the GALEX NUV-Gaia Bp CMD, are depicted in darker purple (168). Over half of the objects that we identify as WDs are not identified as WDs in the Gaia EDR3 filters, indicating that they appear as non-WD-like objects in the Gaia EDR3 filters.

We estimate a value for the reddening in Gaia EDR3 and GALEX filters using a method similar to Gentile Fusillo et al. (2019). An estimated Galactic extinction is identified from the Schlegel et al. (1998) dust map for each object individually. The extinction coefficients for the GALEX filters were derived by Wall et al. (2019), while coefficients similar to Bédard et al. (2020) were utilized for the Gaia EDR3 filters. Formulae for abso-

lute magnitude given the apparent magnitude, distance modulus and extinction (assumed uniform along the line of sight) are shown below.

$$G_{\text{star}} = G_{\text{obs}} - DM - 0.835A_V \left[1 - \exp \left(-\frac{\sin |b|}{200\varpi} \right) \right]$$

$$G_{\text{Bp,star}} = G_{\text{Bp,obs}} - DM - 1.364A_V \left[1 - \exp \left(-\frac{\sin |b|}{200\varpi} \right) \right]$$

$$G_{\text{Rp,star}} = G_{\text{Rp,obs}} - DM - 0.778A_V \left[1 - \exp \left(-\frac{\sin |b|}{200\varpi} \right) \right]$$

Here, G_{obs} is the observed magnitude, A_V is the individual Galactic extinction identified from the Schlegel et al. (1998) dust maps in the V -band, b is the Galactic latitude, and ϖ is the parallax in arcsec. Further details concerning this function can be found in Gentile Fusillo et al. (2019).

2.3. Characterization of WD Single and WDND Systems

Using the processed photometry of the systems, an estimate of the WD mass and age was attempted. WD candidates identified below the Gaia EDR3 optical cut are assumed to be WDs without a companion. These single WD stars were characterized using WD cooling models developed by Bédard et al. (2020). Using Bédard et al. (2020) WD cooling models and initial estimates for the mass and cooling age, photometric models of the system in all potential filters were constructed. These photometric models were compared to the photometric data in a χ^2 test. The mass and cooling age of the WD was allowed to change in order to minimize the χ^2 . The processed photometry and modeled photometry used GALEX FUV NUV bands, Gaia EDR3 bands and all the SDSS filters available. Where data were not present, or a value of 0 was reported, the band or filter data were ignored in the χ^2 minimization. The mass of the secondary star for these objects is reported as 0 in the case of single WDs. The estimated mass of the WD was limited by the models to be within 0.2-1.3 M_{\odot} . The estimated masses and cooling ages were applied to the Bédard et al. (2020) WD cooling models to develop an estimate for the temperature of the WD.

For the WD binary candidates, a similar method χ^2 minimization fit was carried out. However, we modified the minimization to attempt to fit a WD mass, a WD cooling age and a MS or giant secondary mass by adding the modeled photometry of the WD with the modeled photometry of a MS or giant star. Padova isochrones (Bressan et al. 2012) were used to model the MS or giant photometry for the fit. Due to the presence of both high-mass stars and evolved stars in the sequence, two different isochrones were chosen to model the data. A cut was done in the optical regions to divide the evolved stars from the rest of the MS objects. The evolved stars were fitted to an isochrone with an age of 10 billion years. It is assumed that all the evolved stars fit on this one isochrone in order to get a rough estimate of mass for these stars. All the stars in this catalogue were cross-matched with the StarHorse catalogue (Anders et al. 2021) to provide an additional estimate for the mass of the secondary star.

A mass for the single WD fit and binary WD of 0.3 M_{\odot} was used for an initial mass estimate. The expected mass of most WDs is between 0.4-0.6 M_{\odot} . However, a smaller initial mass was used to attempt to identify incidences where the fitting function failed to deviate from the initial mass provided. Figure 4 reveals no such failure to deviate, whereas WDND WD mass estimates showed a significant number of entries that failed to deviate from the initial mass.

A correction had to be applied to our data while attempting to fit GALEX NUV filter for candidate binary systems. When the best fit MS or giant star was chosen out of Gaia EDR3 filters, the modeled GALEX NUV magnitude for the MS or giant star was smaller than the NUV filter data. This means that the secondary star is emitting more NUV light than we expect for a MS or giant star of this type. We attribute this anomaly to poor MS and giant photometry models in the GALEX NUV and exclude the NUV filter in our fits where the anomaly is present.

This catalogue reports the information present in the GALEX and Gaia EDR3 cross-match as well as SDSS DR12 and Pan-STARRS DR1 data, if any are present. It also reports the cross-matched StarHorse catalogue entries as well as the estimated WD mass, WD cooling age and MS star's mass for both DA and DB atmosphere WDs.

3. CATALOGUE CONTENTS

The catalogue contains 444,107 unique candidate WD systems. These systems were identified as candidate WDs using GALEX and Gaia EDR3 data. The first section contains identification information for each star system (Right Ascension and Declination). GALEX data follows the identification section. The GALEX portion of the table contains all the GALEX data for each entry. The Gaia EDR3 section contains information regarding each star based on the Gaia EDR3 data. Pan-STARRS and SDSS DR12 data are listed next. Entries will be empty if the star did not have either Pan-STARRS or SDSS DR12 data to correspond with the Gaia EDR3 data. Entries that were cross-matched to StarHorse (Anders et al. 2021) follow after the SDSS and Pan-STARRS data. The entries having no StarHorse data were left blank. Entries that matched with the Gentile Fusillo et al. (2021) WD catalogue are listed after StarHorse. Following this section are three boolean columns that are true if the star passed our photometry cut for either the GALEX FUV-NUV (fuvwd), GALEX NUV - Gaia EDR3 Bp (nuvwd) and Gaia EDR3 (gaiawd). The final section of the catalogue is the mass estimate of the WD and the non-degenerate star for both DA model estimates and DB model WD estimates. The secondary star column will have an entry of 0 for WDs that are assumed to be without a companion. Entries without a value were reported as 99.9 or 99.0. See Appendix A for a detailed list of all the columns.

4. ANALYSIS

4.1. Single White Dwarfs

A significant portion of our catalogue contains single WDs. An attempt to estimate the mass, temperature and cooling age of the WD was performed using the pho-

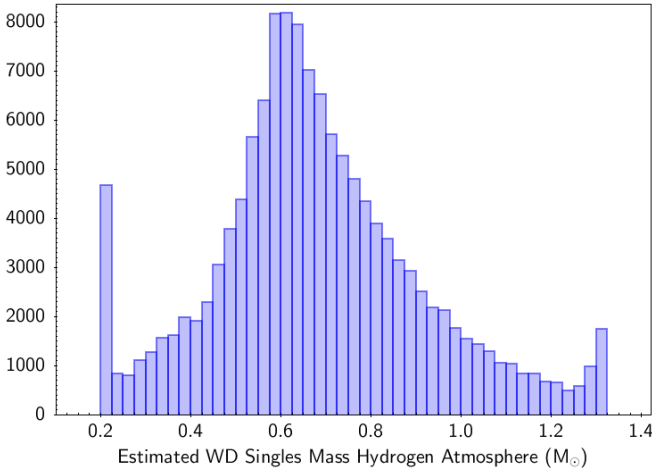


Figure 4. : The estimated mass distribution of WDs identified as WD stars in Gaia filters assuming hydrogen atmospheres (DA models). The sudden spikes on the tails of the distribution are likely WDNDs mixed into the single WD data and did not properly fit our models.

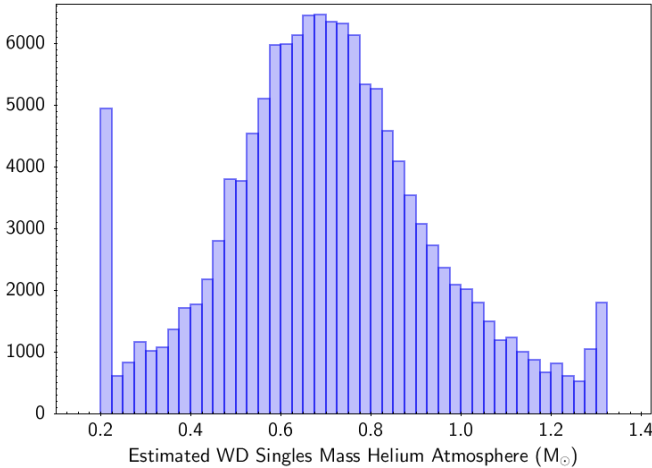


Figure 5. : The estimated mass distribution of WDs identified as WD stars in Gaia filters assuming helium atmospheres (DB models). The sudden spikes on the tails of the distribution are likely WDNDs mixed into the single WD data and did not properly fit our models.

tometric data and non-binary WD models. The mass distribution of these estimates, using DA model assumptions on the WD, can be observed in Figure 4 and using DB model assumptions in Figure 5. The increase in objects at $0.2M_{\odot}$ is likely caused by a fitting failure. This failure may have occurred due to the assumption that the WD is a single star, when in fact these WD systems may be WDND binary systems that were indistinguishable from those on the WD cooling sequence. The area used to define the single WD region is described by the blue area in the lower left corner of Figure 2. One can observe a part of the WDND region is contained within the blue area, giving credibility to the idea that our single WD assumption is not accurate for all these systems. A similar problem may be occurring at $1.3M_{\odot}$. To ensure our fitting function is accurate, we used a cross-match with the Gentile Fusillo et al. (2021) WD catalogue. This

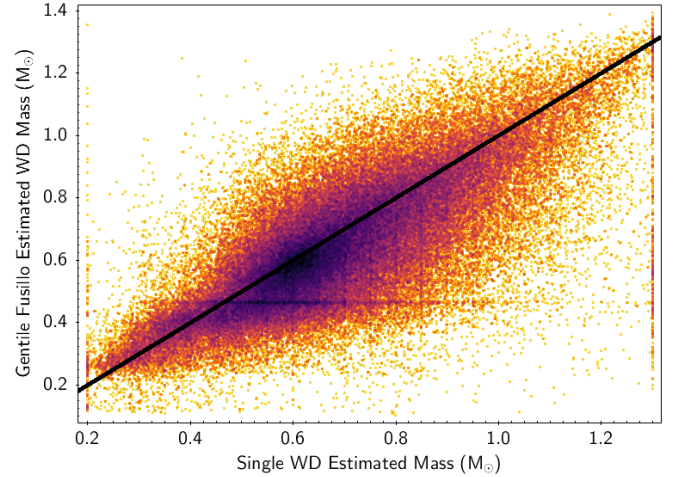


Figure 6. : The estimated WD mass from Gentile Fusillo et al. (2021) WD catalogue compared to the estimated WD mass from our catalogue (DA models). The stars shown in the figure are a one-to-one match with those in the Gentile Fusillo et al. (2021) catalogue and contain only single WDs. The black line describes a one-to-one mass relationship between Gentile Fusillo et al. (2021) and our catalogue’s estimated WD mass.

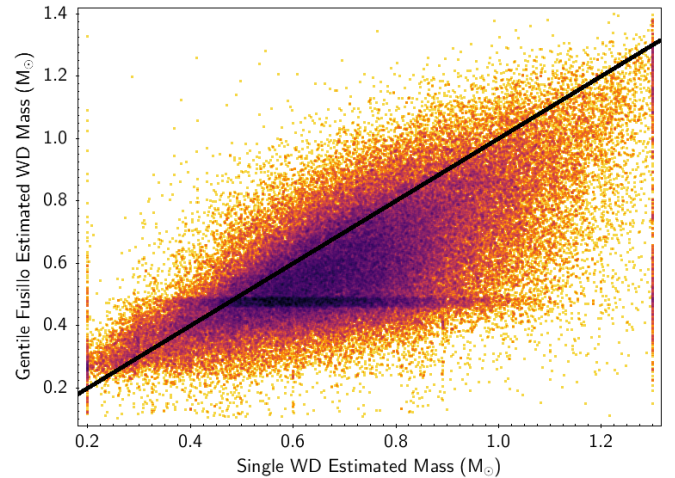


Figure 7. : The estimated WD mass from Gentile Fusillo et al. (2021) WD catalogue compared to the estimated WD mass from our catalogue (DB models). The stars shown in the figure are a one-to-one match with those in the Gentile Fusillo et al. (2021) catalogue and contain only single WDs. The black line describes a one-to-one mass relationship between Gentile Fusillo et al. (2021) and our catalogue’s estimated WD mass.

catalogue is primarily based on single WD systems gathered from Gaia EDR3 and estimates the WD mass in a similar χ^2 minimization analysis. The matched entries were primarily single WDs and represent 111,996 entries in our catalogue. Figure 6 shows the distribution of DA WD mass estimates using GALEX and Gaia EDR3 data compared to the mass reported by Gentile Fusillo et al. (2021). Figure 9 shows the same distribution assuming DB WDs. The distribution of WD masses implies similar WD mass values to those found in Gentile Fusillo et al. (2021) with a few deviations. In Figure 8, the overall dis-

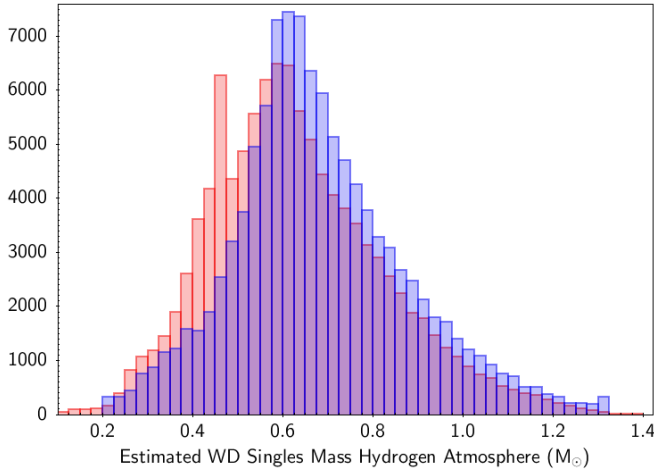


Figure 8. : WD mass distribution of objects that only have entries in the Gentile Fusillo et al. (2021) catalogue (DA models). The blue represents our mass estimate and the orange represents the mass reported by Gentile Fusillo et al. (2021). There is a clear shift to higher mass WDs in our estimated WD mass than those reported in Gentile Fusillo et al. (2021).

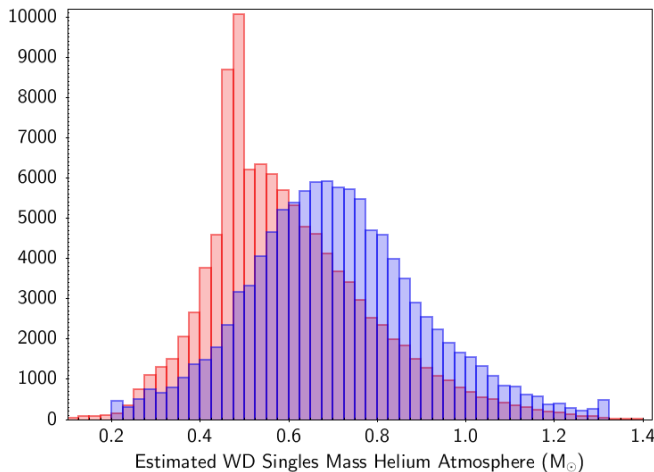


Figure 9. : WD mass distribution of objects that only have entries in the Gentile Fusillo et al. (2021) catalogue (DB models). The blue represents our mass estimate and the orange represents the mass reported by Gentile Fusillo et al. (2021). Similar to Figure 8, there is a clear shift to higher mass WDs in our estimated WD mass than those reported in Gentile Fusillo et al. (2021).

tribution is shifted towards somewhat higher mass WDs when compared to Gentile Fusillo et al. (2021). This discrepancy between the masses in the two catalogues is likely caused by the inclusion of all available photometry from GALEX, SDSS and Gaia EDR3, where Gentile Fusillo et al. (2021) only considers Gaia EDR3 data. There is also an anomaly in the Gentile Fusillo et al. (2021) data that reports an unusually large number of WDs as having a mass of roughly $0.46 M_{\odot}$. The source of this anomaly is unknown. We calculate the reduced χ^2 between our WD mass estimates and Gentile

Fusillo et al. (2021) WD mass estimates

$$\chi_{\text{red}}^2 = \frac{1}{N} \sum_i \left[\frac{(M_{\text{Fusillo, H}} - M_{\text{our, H}})^2}{\sigma_{M, \text{Fusillo, H}}^2 + \sigma_{M, \text{our, H}}^2} \right]$$

over the WDs in both samples excluding the anomalous regions of $0.46 M_{\odot} < M_{\text{Fusillo, H}} < 0.47 M_{\odot}$, $M_{\text{our, H}} < 0.21 M_{\odot}$ and $M_{\text{our, H}} > 1.29 M_{\odot}$ and obtain 2.5. The median value reported by our WD mass estimates excluding the anomalous regions is 0.66 and the median value reported by Gentile Fusillo et al. (2021) is 0.62, leading to a difference of 0.04. These values indicate that the WD mass estimates from our catalogue and Gentile-Fusillo catalogue generally agree within their respective uncertainties.

The WD DA estimated masses reported by Gentile Fusillo et al. (2021) are plotted onto both Gaia EDR3 CMDs and GALEX CMDs in the top two plots, alongside our estimates for DA WDs on the bottom two plots of Figure 10. The bottom left plot in Figure 10 depicts single WDs with a broader distribution of WDs between $0.6-0.8 M_{\odot}$ compared to the top left plot. In the top right plot, there is a far less homogeneous distribution in the UV for the reported values of WDs in Gentile Fusillo et al. (2021). In particular, the high mass WD region has a high degree of scatter. However, in the bottom right plot of Figure 10 there is a spread of mass in the WDs with closer consistency to modeled WD masses. A similar pattern is observed with the DB WDs in Figure 11. It is uncertain how accurate the GALEX UV data is when predicting the WD masses, but Figure 10 indicates that there is a significant change when including UV data.

By construction, each object in our catalogue has a measured UV flux either in the NUV or the FUV. This information clearly influences the masses determined through the fitting process as our fitted masses better correlate with a star's position in the UV CMD than the masses from Gentile Fusillo et al. (2021) as shown in Fig. 10 and 11. The additional UV data provides both an opportunity in that the UV fluxes depend strongly on the temperature of the white dwarfs and a potential pitfall in that the observed UV fluxes typically have larger statistical and systematic uncertainties than the Gaia DR3 fluxes. As Fig. 6 through 9, our fitted masses (whether using DA or DB models) are systematically slightly larger than those obtained by Gentile Fusillo et al. (2021). Adding the UV data to the visual data from Gaia used by Gentile Fusillo et al. (2021) may yield more accurate temperature estimates and, therefore, more accurate mass estimates. However, there is a bias in that the GALEX flux measurements have larger uncertainties than the Gaia measurements. These uncertainties, when combined with the flux distribution of WDs (fainter WDs), will systematically cause the UV fluxes to be overestimated, thereby the temperatures also to be overestimated and finally also the masses to be overestimated.

4.2. White Dwarfs in Binaries

WDND WD mass estimates were less successful than single WD mass estimates. A large portion of the WD mass estimates for WDNS systems were approximately $0.2 M_{\odot}$, $0.3 M_{\odot}$ and $1.3 M_{\odot}$. The large fraction of WD estimates at $0.3 M_{\odot}$ is related to the initial guess used in

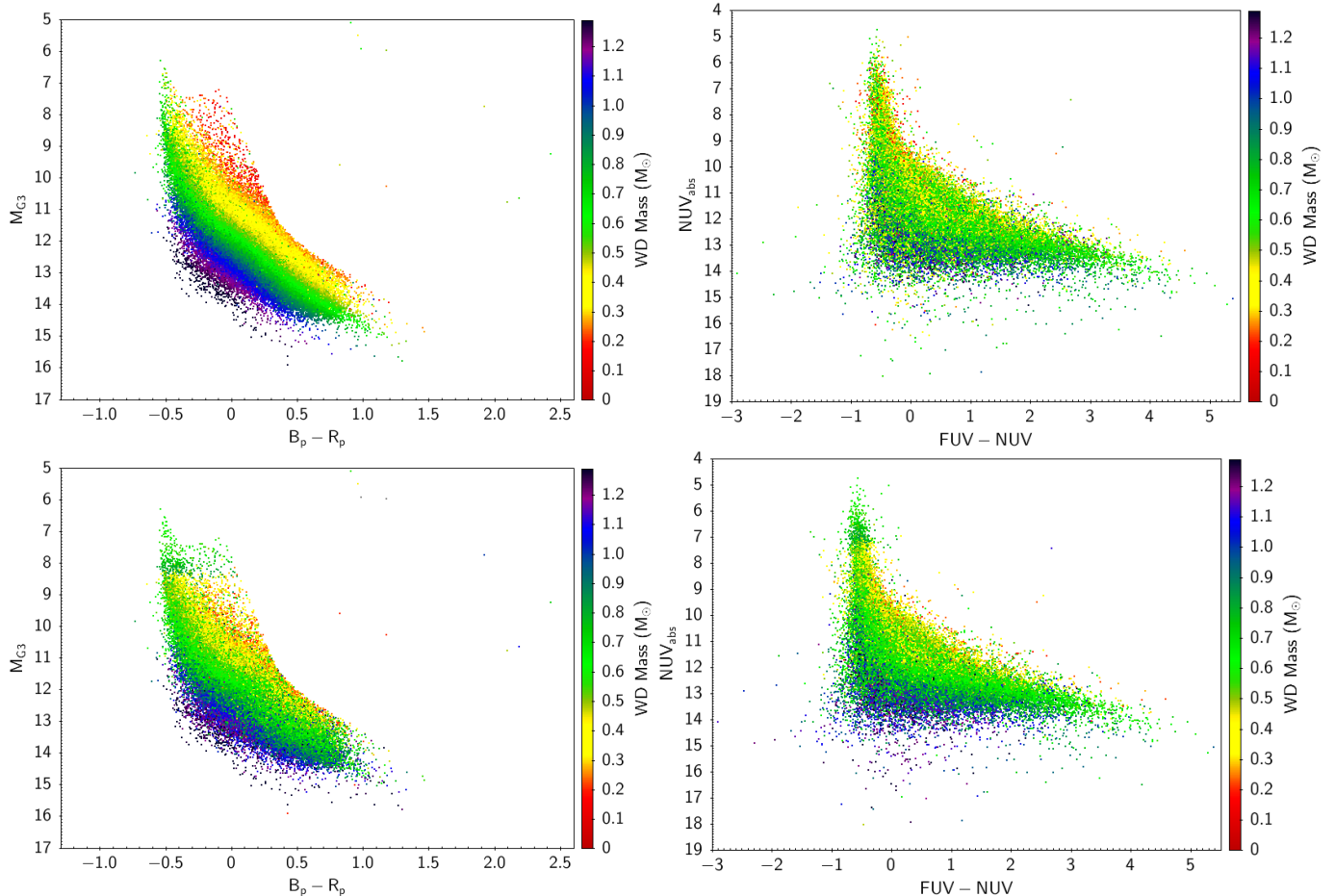


Figure 10. : The four figures above depict the mass distribution of single WD stars in our catalogue that were previously identified in Gentile Fusillo et al. (2021) with hydrogen DA models. The top two figures depict the mass distribution reported by Gentile Fusillo et al. (2021) for both the visual magnitude in Gaia EDR3 on the left and the UV magnitude in GALEX on the right. The two bottom figures depict the mass distribution of WDs that we estimated considering the UV magnitude. The left figure depicts the visual magnitude in Gaia EDR3 on the left and the UV magnitude in GALEX on the right.

the χ^2 fitter for the WD mass which was given as $0.3M_{\odot}$. All three values are failed WD mass estimates where the fitter was unable to gather reliable mass estimates. In areas outside these three values, the masses returned by our fitting were uniform over the allowed range in the fitting. The WD model takes up any UV excess in the data relative to the MS model, so discrepancies in the UV data, the MS or giant models, the WD models or all three yield inaccurate WD mass estimates. As stated in Section 2.3, the models used to calculate the GALEX NUV output of MS stars fitted with Gaia EDR3 data exhibited considerably more NUV emission than observed. Consequently, it is likely that the poor reliability of many of our estimates is related to a lack of suitable models for the GALEX FUV and NUV magnitudes of the stars. We cannot estimate the mass of WDs in WDNDs with photometry alone and spectra are required to have certainty of WDND WD mass estimates.

These WDND candidates are MS or evolved stars whose photometry exhibits a UV excess similar to WD stars. If these are WDND systems, we expect the WD UV magnitude to either dominate the UV light observed or have an additional contribution of UV flux from the

non-degenerate star. This would move the object off the WD sequence described below the black line in the left plot of Figure 1 and toward the top right of the figure. Below the WD region depicted in the left plot of Figure 1, the catalogue does not likely contain high mass WDs. Instead, there is a possibility that these are low flux readings from MS stars or flaring M-dwarf stars. This is consistent with SDSS spectra classifications shown in Figure 16 where M-dwarf stars are identified in our catalogue based on their UV data, not their optical data. This suggests that a certain fraction of the catalogue contains M-dwarf stars with excess UV. A χ^2 minimization fit was performed to attempt to identify the masses of these non-degenerate systems assuming a potential WD was contributing to the UV flux. The distribution of non-degenerate mass estimates can be seen in Figure 12. A cross-match with the StarHorse MS catalogue (Anders et al. 2021) was performed to supplement our non-degenerate mass estimates. Of the 309,584 entries, 193,221 objects matched to StarHorse and reported a non-degenerate mass estimate. Figure 14 describes the difference between our non-degenerate mass estimates and StarHorse’s reported MS mass. The black

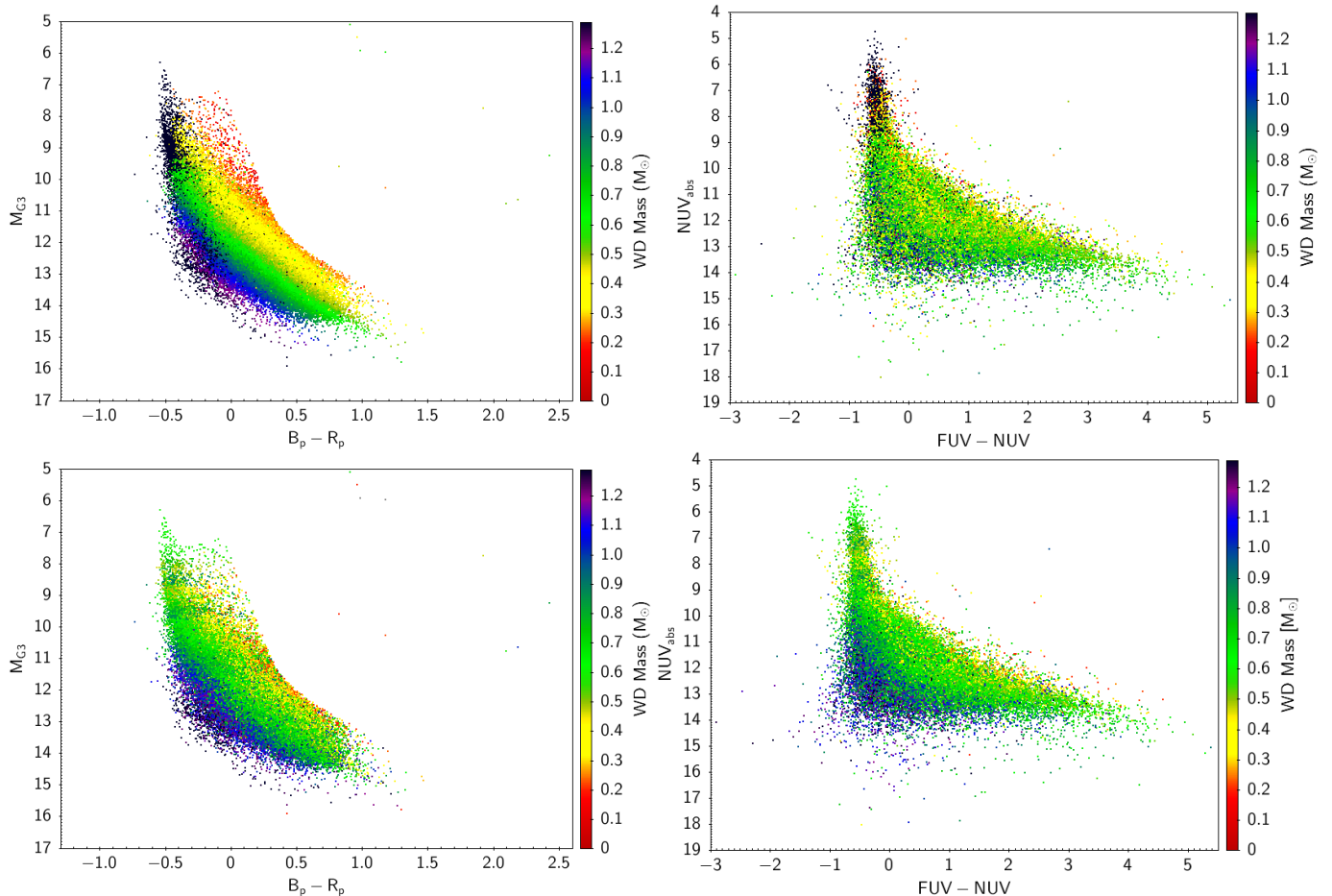


Figure 11. : The four figures above depict the mass distribution of single WD stars in our catalogue that were previously identified in Gentile Fusillo et al. (2021) to have helium DB models. The top two figures depict the mass distribution reported by Gentile Fusillo et al. (2021) for both the visual magnitude in Gaia EDR3 on the left and the UV magnitude in GALEX on the right. The two bottom figures depict the mass distribution of WDs that we estimated considering all available photometric data. The left figure depicts the visual magnitude in Gaia EDR3 and the UV magnitude in GALEX on the right.

line in the figure represents a one-to-one relationship. The stars above the black line are stars where StarHorse reported masses higher than our own estimates and below the black line represents stars where StarHorse reported a lower mass than our estimates. From Figure 14, there exists a one-to-one correlation between our estimated masses and the StarHorse reported masses up until $0.9 M_{\odot}$. A discontinuity exists at $1.04 M_{\odot}$. This is a known degeneracy in our fitting caused by the upper mass limit of one of the isochrones used. In order to develop a complete look at the non-degenerate mass distribution of the catalogue, we utilize a mass cut. For stars with masses greater than $0.9 M_{\odot}$, StarHorse is likely the more accurate estimate for the non-degenerate mass. This is due to the uncertainty in the UV flux of the models we used, whereas for stars less massive than $0.9 M_{\odot}$, we assume that StarHorse will incorrectly estimate the mass of the non-degenerate star if there is a WD in the system. This is due to the non-degenerate star being faint enough to allow for the WD to contribute significantly to the visual flux of the system. Figure 15 depicts the distribution of non-degenerate star masses using our mass estimates for non-degenerate stars with a mass less

than $0.9 M_{\odot}$ (shown in blue) and StarHorse mass estimates for stars with a mass greater than $0.9 M_{\odot}$ (shown in orange). The slopes of the non-degenerate mass distribution of Figure 15 change considerably. On the low mass end, the slope incrementally increases, then flattens out to an exponent of 1.4. A dearth of objects exists at $0.65 M_{\odot}$. On the high mass end, the distribution displays another sudden lack of objects at around $1.5 M_{\odot}$. After the dip, the slope of the distribution is a -4 exponent before becoming a slope of -8 exponent. We calculate that for binary systems where one star has evolved into a WD, the initial mass function (IMF) should tend toward a slope of -7.5 exponent. Moe & Di Stefano (2017) reported that in recent observations of binary systems IMFs with smaller mass ratios (0.1-0.3), the power-law of the mass ratio distribution flattens towards shallower slopes.

4.3. SDSS Spectroscopy

All entries with available SDSS photometry and spectral data have been included in the catalogue. A total of 11,607 entries have SDSS spectral classifications. Figure 16 depicts the distribution of the various spectral types

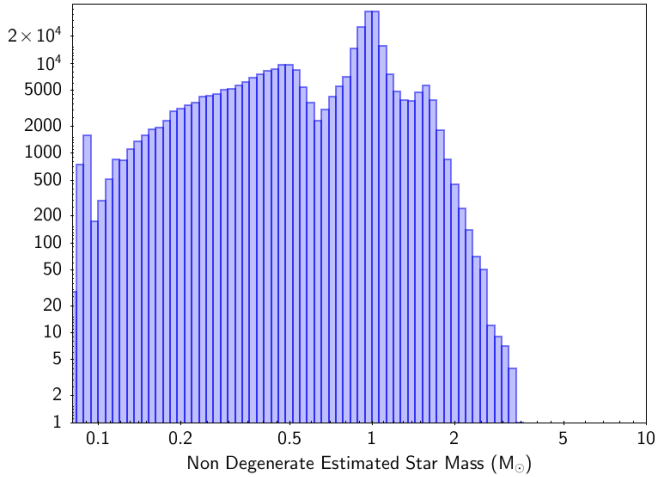


Figure 12. : The distribution of mass estimates of non-degenerate stars with a WD companion contributing to the UV of the system. For objects above $0.9 M_{\odot}$, the distribution of estimated stellar mass becomes unreliable. This is due to the assumed WD in the system dominating the UV, forcing the non-degenerate mass estimate to be smaller than what can be seen in the optical. There is also a discontinuity in our fitting due to the difficulty with the isochrones for giant stars that can be observed as the peaks in Figure 14.

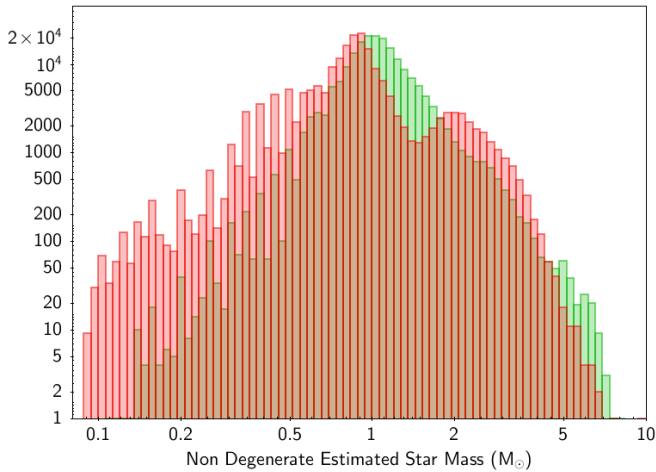


Figure 13. : Comparison of the StarHorse mass distribution of stars found in our candidate WDND systems correlate to the red distribution. A general distribution of StarHorse main sequence masses are observed in green. Each distribution contains the same number of stars. For objects below $0.9 M_{\odot}$, the distribution of estimated stellar mass becomes unreliable. This is due to the StarHorse catalogue assuming that the system is a single star system.

identified by SDSS. The distribution of SDSS classifications is heavily biased to WD identifications with 6,432 of the 11,607 objects being single WDs. Of the remaining entries, 1,151 were listed as cataclysmic variables (CVs). These objects can be seen in the Gaia EDR3 CMD in Figure 17. There is a clear concentration of objects identified as CVs on the WD sequence. Upon investigating their spectra, a large portion of these objects do not appear to

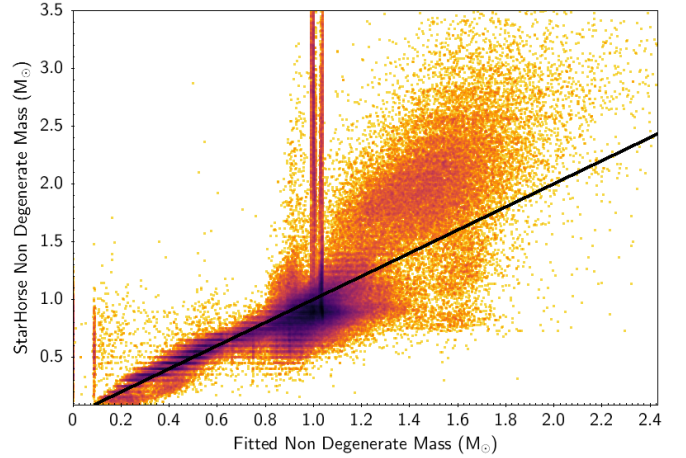


Figure 14. : Comparison of the difference in our fitted secondary star masses and masses in StarHorse. The black line describes the situation where the mass we have fitted perfectly matches the StarHorse mass. Objects below the black line are stars where we fit to higher masses than StarHorse and above the black line are stars where we fit a smaller mass than StarHorse. The spiked lines at $1M_{\odot}$ and $1.04M_{\odot}$ are known issues with the isochrones used being incapable of correctly estimating the mass of evolved stars.

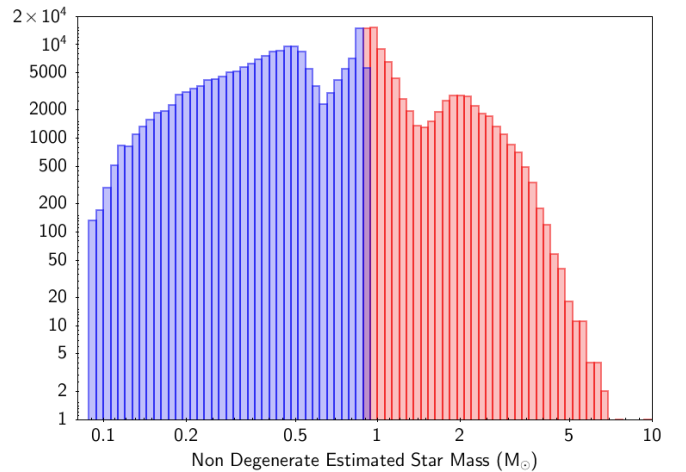


Figure 15. : This distribution represents our estimated non-degenerate mass in the blue with StarHorse estimated mass in the red from $0.09 M_{\odot}$ to $9.53 M_{\odot}$. A cutoff between the two distributions is performed at $0.9 M_{\odot}$ where we believe that StarHorse MS mass estimates will be less reliable below $0.9 M_{\odot}$ due to the presence of a WD in the system.

have clear emission lines. The SDSS DR12 website provides the following caveat: “Although sub-classifications are provided, they are not optimized for accuracy. In particular, the CV star templates have more degrees of freedom than other stellar templates, which can result in unphysical solutions where negative PCA components of the CV templates can fit absorption features of White Dwarfs” (Aguado et al. 2015). It is unlikely that the 1,151 listed CVs are accurately identified; therefore, a significant portion of CVs listed are likely single WDs. A total of 270 or 2.3 percent of the SDSS entries that

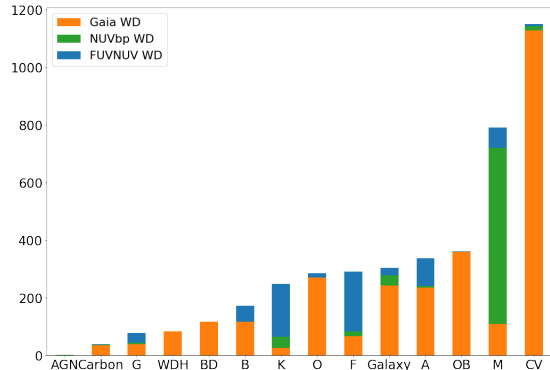


Figure 16. : The distribution of the 11,607 different SDSS DR12 spectral classifications. There are 6,432 WD spectral classifications that are not listed in the figure above. The orange depicts the distribution of SDSS classifications that appear to be WDs in Gaia EDR3 photometry, the green depicts the distribution of objects with SDSS classification that appear to be WDs in the GALEX NUV and Gaia EDR3 Bp region and the blue depicts the SDSS classification that appear to be WDs in the GALEX photometry alone. The distribution is dominated by over 6,000 WD identifications which are not depicted in histogram.

matched with our catalog were listed as galaxies. Using the SDSS optical spectrum archive, we examined the top ten galaxy entries with the highest signal-to-noise ratio to further understand if there was a large contaminant of galaxies in our data. Of these ten entries, nine were misidentified. Spectra with clear WD features often have their hydrogen absorption lines misidentified as oxygen II emission lines, giving several entries a consistent redshift of roughly 0.7. There is also misidentification of M-dwarf stars as galaxies due to the presence of H_α and H_β in the spectrum. The presence of the hydrogen spectral lines in the M-dwarf spectra likely causes the spectral identifier to assume the system contains many stars and is, thus, a galaxy. It is also likely that the source of these hydrogen spectral lines could be coming from a WD in the system and not a star-rich galaxy. Furthermore, several entries had a redshift close to zero or were actually negative, meaning they are likely misidentified stars, not galaxies. After examining the spectra of the 270 listed galaxies, it seems that a large fraction of them are misidentified sources. It is worth noting that these 270 objects make up only a tiny fraction of the 791,977 galaxy identifications in the SDSS DR12 catalogue (Alam et al. 2015).

5. CONCLUSIONS

The aim of the GALEX-Gaia-EDR3 catalogue is to identify and characterise candidate white-dwarf-non-degenerate binary stars to be used for additional study or for follow-up observation. The GALEX-Gaia-EDR3 catalogue was constructed from GALEX and Gaia EDR3 catalogues containing 332,111 candidate white dwarf binary systems and 111,996 candidate single white dwarfs. When available, data from SDSS DR12, Pan-STARRS DR1, StarHorse MS catalogue and Gentile-Fusillo Gaia

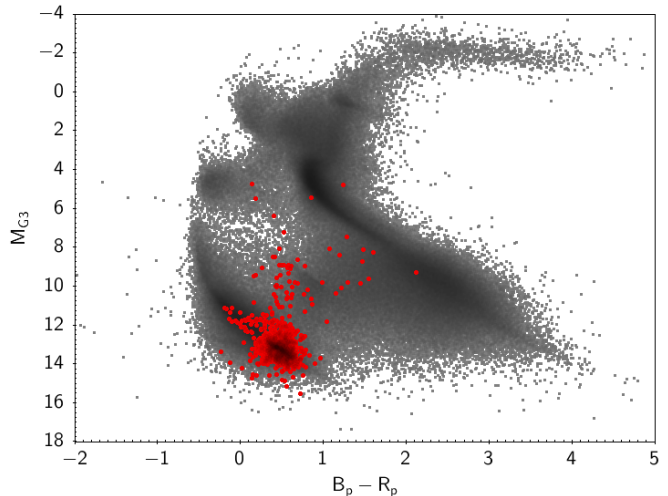


Figure 17. : The depiction of CV objects in our catalogue CMD in Gaia EDR3 magnitudes. All objects in the catalogue are marked in grey. The red points mark the objects that were classified by SDSS DR12 as CVs.

EDR3 white dwarf catalogue augment the catalogue to provide supplementary data. Estimates for the white dwarf’s mass, age, effective temperature and the non-degenerate secondary mass were determined through fitting the photometry of objects in our catalogue with modeled white dwarf cooling sequences from Bédard et al. (2020). Upon comparing our results with the 111,996 candidate single white dwarfs with the Gentile-Fusillo Gaia EDR3 white dwarf catalogue, we found that our estimates for the single white dwarf’s mass tended to be skewed slightly towards higher-mass white dwarfs, but generally agree within their respective uncertainties. Mass estimates for the white dwarfs in binary systems have a high degree of inaccuracy due to the presence of the non-degenerate star significantly contributing to the photometry of the system.

ACKNOWLEDGEMENTS

This research has made use of the VizieR catalogue access tool, CDS, Strasbourg, France (DOI : 10.26093/cds/vizieR). The original description of the VizieR service was published in 2000, *A&AS* 143, 23

This work has made use of data from the European Space Agency (ESA) mission *Gaia* (<https://www.cosmos.esa.int/gaia>), processed by the *Gaia* Data Processing and Analysis Consortium (DPAC, <https://www.cosmos.esa.int/web/gaia/dpac/consortium>). Funding for the DPAC has been provided by national institutions, in particular the institutions participating in the *Gaia* Multilateral Agreement.

Funding for SDSS-III has been provided by the Alfred P. Sloan Foundation, the Participating Institutions, the National Science Foundation, and the U.S. Department of Energy Office of Science. The SDSS-III web site is <http://www.sdss3.org/>.

SDSS-III is managed by the Astrophysical Research Consortium for the Participating Institutions of the SDSS-III Collaboration including the University of Arizona, the Brazilian Participation Group, Brookhaven National Laboratory, Carnegie Mellon University, Uni-

versity of Florida, the French Participation Group, the German Participation Group, Harvard University, the Instituto de Astrofísica de Canarias, the Michigan State/Notre Dame/JINA Participation Group, Johns Hopkins University, Lawrence Berkeley National Laboratory, Max Planck Institute for Astrophysics, Max Planck Institute for Extraterrestrial Physics, New Mexico State University, New York University, Ohio State University, Pennsylvania State University, University of Portsmouth, Princeton University, the Spanish Participation Group, University of Tokyo, University of Utah, Vanderbilt University, University of Virginia, University of Washington, and Yale University.

DATA AVAILABILITY

The catalogue presented in this work can be downloaded [HERE](https://doi.org/10.5281/zenodo.8145200) or at the url: <https://doi.org/10.5281/zenodo.8145200>. The catalogue will also be made available via the VizieR Service for Astronomical Catalogues. The original data in this article is publicly available from the relevant survey archives.

REFERENCES

Aguado D. S., et al., 2015, SDSS DR12 Optical Spectra Caveats, https://www.sdss4.org/dr12/spectro/caveats/#stellar_classifications

Alam S., et al., 2015, *ApJS*, 219, 12
 Anders F., et al., 2021, arXiv e-prints, p. arXiv:2111.01860
 Bédard A., Bergeron P., Brassard P., Fontaine G., 2020, *ApJ*, 901, 93
 Bergeron P., Ruiz M. T., Leggett S. K., 1997, *ApJS*, 108, 339
 Bergeron P., Dufour P., Fontaine G., Coutu S., Blouin S., Genest-Beaulieu C., Bédard A., Rolland B., 2019, *ApJ*, 876, 67
 Bressan A., Marigo P., Girardi L., Salasnich B., Dal Cero C., Rubele S., Nanni A., 2012, *MNRAS*, 427, 127
 Gaia Collaboration et al., 2021, *A&A*, 649, A1
 Gentile Fusillo N. P., et al., 2019, *MNRAS*, 482, 4570
 Gentile Fusillo N. P., et al., 2021, *MNRAS*, 508, 3877
 Ivanova N., et al., 2013, *A&A Rev.*, 21, 59
 Lindgren L., et al., 2018, *A&A*, 616, A2
 Martin D. C., et al., 2005, *ApJL*, 619, L1
 Moe M., Di Stefano R., 2017, *ApJS*, 230, 15
 Rebassa-Mansergas A., Agurto-Gangas C., Schreiber M. R., Gänsicke B. T., Koester D., 2013, *MNRAS*, 433, 3398
 Rebassa-Mansergas A., Ren J. J., Parsons S. G., Gänsicke B. T., Schreiber M. R., García-Berro E., Liu X. W., Koester D., 2016, *MNRAS*, 458, 3808
 Rebassa-Mansergas A., et al., 2021, *MNRAS*, 506, 5201
 Ren J. J., Rebassa-Mansergas A., Parsons S. G., Liu X. W., Luo A. L., Kong X., Zhang H. T., 2018, *MNRAS*, 477, 4641
 Schlegel D. J., Finkbeiner D. P., Davis M., 1998, *ApJ*, 500, 525
 Wall R. E., Kilic M., Bergeron P., Rolland B., Genest-Beaulieu C., Gianninas A., 2019, *MNRAS*, 489, 5046
 Willems B., Kolb U., 2004, *A&A*, 419, 1057

APPENDIX

COLUMN DESCRIPTIONS

ra_epoch2000, Right Ascension of the object taken from Gaia at Epoch2000
 dec_epoch2000, Declination of the object taken from Gaia at Epoch2000
 ra_epoch2000_error, Error of the Right Ascension of the object taken from Gaia at Epoch2000
 dec_epoch2000_error, Error of the Declination of the object taken from Gaia at Epoch2000
 ra_dec_epoch2000_corr, Correlation between right ascension and declination
 source_id, a Unique source identifier within a Gaia data release
 name, GALEX object name
 objid, GALEX identifier in JHHMMSS.s+DDMMSS format
 Cat, Survey type (Always AIS-all-sky imaging survey)
 FUVexp, FUV exposure time.
 NUVexp, NUV exposure time
 GLON, Galactic Longitude
 GLAT, Galactic Latitude
 tile, Title number
 img, Image number
 sv, Number of subsists if exposure was divided
 r.fov, Distance of source from center of the field
 Obs, Observation type
 b, Bands: 1=NUV, 2=FUV, 3 both
 E(B-V), Galactic reddening inferred from 100um dust emission maps (E_bv)
 Sp?, 1 if a spectrum exists (istherespectrum)
 chkf, Astrometry check type
 FUVmag, Galex FUV Calibrated magnitude in AB system
 e_FUVmag, FUV mag error
 NUVmag, Galex NUV calibrated magnitude in AB system
 e_NUVmag, NUV mag error
 FUV.a, FUV Kron-like elliptical aperture magnitude
 e_FUV.a, FUV RMS error for AUTO magnitude
 NUV.a, NUV Korn-like elliptical aperture
 e_NUV.a, NUV RMS error for AUTO magnitude
 FUV.4, FUV mag aperture 8 pix diameter
 e_FUV.4, FUV mag aperture error (8 pix diameter)
 NUV.4, NUV mag aperture (8 pix diameter)

e.NUV.4, NUV mag aperture error (8 pix diameter)
 FUV.6, FUV mag aperture (17 pix diameter)
 e.FUV.6, FUV mag aperture error (17 pix diameter)
 NUV.6, NUV mag aperture (17 pix diameter)
 e.NUV.6, NUV mag aperture error (17 pix diameter)
 Faf1, FUV artifact Flag (logical OR near source)
 Naf1, NUV artifact Flag (logical OR near source)
 Fexf, Extraction flags for FUV band
 Nexf, Extraction flags for NUV band
 Fflux, FUV calibrated Flux
 e.Fflux, FUV flux error
 Nflux, NUV calibrated flux
 e.Nflux, NUV flux error
 FXpos, Source position in FUV image along x
 FYpos, Source position in UV image along y
 NXpos, Source position in NUV image along x
 NYpos, Source position in NUV image along y
 Fima, Source FWHM in FUV assuming a gaussian core
 Nima, Source FWHM in NUV assuming a gaussian core
 Fr, Source FWHM in FUV assuming a gaussian core
 Nr, Source FWHM in NUV assuming a gaussian core
 nS/G, Star/galaxy classifier from NUV
 fS/G, Star/galaxy classifier from FUV
 nell, 1-b/a in NUV
 fell, 1-b/a in FUV
 nPA, Position angle in NUV
 e.nPA, Position angle error in NUV
 fPA, Position angle in FUV
 e.fPA, Position angle error in FUV
 Fnr, FUV FWHM IMAGE value from -fd-ncat.fits
 F3r, FUV flux radius
 Nar, Kron apertures in units of a or b for NUV
 Narms, Profile RMS along major axis for NUV
 Nbrms, Profile RMS along minor axis for NUV
 Far, Kron apertures in units of a or b for FUV
 Farms, Profile RMS along major axis for FUV
 Fbrms, Profile RMS along minor axis for FUV
 w_NUV, NUV effective exposure (flat-field response value) at the source position
 w_FUV, FUV effective exposure
 Prob, Probability of the FUVxNUV match
 Sep, Separation between FUV and NUV position of the source in the same observation
 Nerr, Position error of the source in the NUV image
 Ferr, Position error of the source in the FUV image
 Ierr, Inter-band position error
 Nperr, NUV poisson position error
 Fperr, FUV poisson position error
 CV, Whether the source comes from a coda or visit. (corv)
 G, Neighbours rank
 N, Number of sources within 2.5", if this is a primary.
 primid, objid of the closest primary, based on distance criterion
 groupid, Objid's of all sources (AIS) within 2.5", concatenated by "+"
 Gd, as for "G" (grank), but based on distance criterion (granddist)
 Nd, as for "N" (ngrank), but based on distance criterion
 OName, Extended object if not:"N"
 parallax, Absolute stellar parallax
 parallax_error, standard error of parallax
 pm, Total proper motion (pm)
 pmra, proper motion in right ascension direction
 pmra_error, standard error of proper motion in right ascension direction
 pmdec, proper motion in declination direction
 pmdec_error, standard error of proper motion in declination direction
 astronomic_n_good_obs_al, number of good observations AL
 astronomic_gof_al, Goodness of fit statistic of model wrt along-scan observations
 astrometric_chi2_al, AL chi-squared value

astrometric_excess_noise, Excess noise of the source
 astrometric_excess_noise_sig, Significance of excess noise
 astrometric_params_solved, Which parameters have been solved for
 pseudocolour, astrometrically determined pseudo colour of the source
 pseudocolour_error, standard error of pseudo color of source
 visibility_periods_used, Number of visibility periods used in astronomic solution
 ruwe, Gaia dr2 re-normalised unit-weight error (Lindgren et al. 2018)
 duplicated_source, Source with duplicate sources
 phot_g_mean_flux, Mean G Flux
 phot_g_mean_flux_error, Mean G Flux error
 phot_g_mean_mag, mean G magnitude
 phot_g_mean_mag_error, Mean G magnitude error
 phot_bp_mean_flux, Integrated mean flux in BP band
 phot_bp_mean_flux_error, Error of the integrated BP mean flux
 phot_bp_mean_mag, Integrated BP mean magnitude (Vega)
 phot_bp_mean_mag_error, error of the integrated BP mean magnitude
 phot_rp_mean_flux, Integrated RP mean flux
 phot_rp_mean_mag, Integrated RP mean magnitude (Vega)
 phot_rp_mean_mag_error, error on integrated RP mean magnitude
 phot_bp_rp_excess_factor, BP/RP excess factor
 bp_rp, BP-RP Gaia colour
 phot_g_mean_mag_corrected, Calibration corrected G magnitude (added by CDS)
 phot_g_mean_mag_error_corrected, Standard error of calibration corrected G magnitude (added by CDS)
 phot_g_mean_flux_corrected, Calibration corrected G-band mean flux (added by CDS)
 phot_bp_rp_excess_factor_corrected, Calibration corrected BP/RP excess factor (added by CDS)
 dr2_radial_velocity, Radial velocity from Gaia DR2
 dr2_radial_velocity_error, Radial velocity error from Gaia DR2
 dr2_rv_nb_transits, Number of transits used to compute radial velocity in Gaia DR2
 dr2_rv_template_teff, Teff of the template used to compute radial velocity in Gaia DR2
 dr2_rv_template_logg, logg of the template used to compute radial velocity in Gaia DR2
 urat1, URAT1 cross-id name (urat1)
 objID_psd1, Unique object identifier for Pan-STARRS
 f_objID_psd1, Information flag bitmask indicating details of the photometry.
 Qual_psd1, Subset of objInfoFlag denoting whether this object is real or likely false positive.
 Epoch_psd1, Modified Julian date of the mean Epoch
 Ns_psd1, Number of stack detection
 gmag_psd1, Mean PSF AB magnitude from g filter (4866 angstroms) detection
 e_gmag_psd1, error in gmag
 gKmag_psd1, mean Kron AB magnitude from g filter detection
 e_gKmag_psd1, error in gKmag
 gFlags_psd1, Information flag bitmask for mean object from g filter detection
 rmag_psd1, Mean PSF AB magnitude from r filter (6215 angstroms) detection.
 e_rmag_psd1, error in rmag
 rKmag_psd1, Mean Kron AB magnitude from r filter detection
 e_rKmag_psd1, Error in rKmag
 rFlags_psd1, Information flag bitmask fro mean object from r filter detection
 imag_psd1, mean PSF AB magnitude from i filer (7545 angstroms) detection.
 e_imag_psd1, error in imag
 iKmag_psd1, Mean Kron AB magnitude from i filter detection
 e_iKmag_psd1, error in iKmag
 iFlags_psd1, Information flag bitmask fro mean object from i filter detection
 zmag_psd1, Mean PSF AB magnitude from z filter (8679 angstroms) detection
 e_zmag_psd1, error in zmag
 zKmag_psd1, Mean Kron AB magnitude from z filter detection
 e_zKmag_psd1, Error in zKmag
 zFlags_psd1, Information flag bitmask for mean object from z filter detection
 ymag_psd1, Mean PSF AB magnitude from y filter (9633 angstroms) detection
 e_ymag_psd1, Error in ymag
 yKmag_psd1, Mean Kron AB magnitude from y filter detection
 e_yKmag_psd1, error in yKmag
 yFlags_psd1, Information flag bitmask for mean object from y filter detection
 objID_sdssdr12, SDSS unique object identifier
 mode_sdssdr12, 1: primary (469,053,874 sources), 2: secondary (324,960,094 sources)
 q_mode_sdssdr12, '+' indicates clean photometry (310,190,812 sources with mode 1+) (clean)

class_sdssdr12, Type of object (3=galaxy, 6=star)
SDSS12_sdssdr12, SDSS-DR12 name, based on J2000 position
m_SDSS12_sdssdr12, The asterisk indicates that 2 different SDSS objects share the same SDSS12 name
flags_sdssdr12, Photo Object Attribute flags
ObsDate_sdssdr12, Mean Observation date
Q_sdssdr12, Quality of the observation
umag_sdssdr12, model magnitude in u filter, AB scale
e_umag_sdssdr12, mean error on umag
gmag_sdssdr12, model magnitude in g filter, AB scale
e_gmag_sdssdr12, Mean Error on gmag
rmag_sdssdr12, Model magnitude in r filter, AB scale
e_rmag_sdssdr12, Mean error on rmag
imag_sdssdr12, Model magnitude in i filter, AB scale
e_imag_sdssdr12, Mean error on imag
zmag_sdssdr12, Model magnitude in z filter, AB scale
e_zmag_sdssdr12, Mean error on zmag
zsp_sdssdr12, Spectroscopic redshift (when SpObjID_i0)
e_zsp_sdssdr12, Mean error on zsp
f_zsp_sdssdr12, “zwarning” flag
zph_sdssdr12, Photometric redshift; estimated by robust fit to nearest neighbors in a reference set.
e_zph_sdssdr12, estimated error of the photometric redshift
avg_zph_sdssdr12, Average redshift of the nearest neighbors; if significantly different from mph this might be a better estimate than zph.
pmRA_sdssdr12, Proper motion along Right Ascension
e_pmRA_sdssdr12, Mean error on pmRA
pmDE_sdssdr12, Proper motion along Declination
e_pmDE_sdssdr12, mean error on pmDE
SpObjID_sdssdr12, Pointer to the spectrum of object or 0
spType_sdssdr12, Source type (sourceType)
spCL_sdssdr12, Spectroscopic class: GALAXY, QSO, STAR
subClass_sdssdr12, spectroscopic subclass
dist05, StarHorse distance, 5th percentile
dist16, StarHorse distance, 16th percentile
dist50, StarHorse distance, 50th percentile
dist84, StarHorse distance, 85th percentile
dist95, StarHorse distance, 95th percentile
av05, StarHorse line-of-sight extinction at lambda = 5420 angstrom, 5th percentile
av16, StarHorse line-of-sight extinction at lambda = 5420 angstrom, 16th percentile
av50, StarHorse line-of-sight extinction at lambda = 5420 angstrom, 50th percentile
av84, StarHorse line-of-sight extinction at lambda = 5420 angstrom, 84th percentile
av95, StarHorse line-of-sight extinction at lambda = 5420 angstrom, 95th percentile
teff16, StarHorse effective temperature, 16th percentile
teff50, StarHorse effective temperature, 50th percentile
teff84, StarHorse effective temperature, 84th percentile
logg16, StarHorse Surface Gravity, 16th Percentile
logg50, StarHorse Surface Gravity, 50th Percentile
logg84, StarHorse Surface Gravity, 84th Percentile
met16, StarHorse metallicity, 16th percentile
met50, StarHorse metallicity, 50th percentile
met84, StarHorse metallicity, 84th percentile
mass16, StarHorse Stellar Mass, 16th Percentile
mass50, StarHorse Stellar Mass, 50th Percentile
mass84, StarHorse Stellar Mass, 84th Percentile
‘fidelity’, Gaia EDR3 astrometric fidelity flag (Rybizki et al., 2021, MNRAS, in prep.)
TeffH, Effective temperature from fitting the dereddened G, BP, and RP absolute fluxes with pure-H model atmospheres (teff_H), from Gentile Fusillo et al. (2021)
e_TeffH, Uncertainty of teff_H (eteff_H), from Gentile Fusillo et al. (2021)
loggH, Log of surface gravity from the dereddened G, BP, and RP absolute fluxes with pure-H model atmospheres (logg_H) from Gentile Fusillo et al. (2021)
e_loggH, Uncertainty on logg_H (elogg_H), from Gentile Fusillo et al. (2021)
MassH, Stellar mass resulting from the adopted mass-radius relation and best fit parameters (mass_H), from Gentile Fusillo et al. (2021)
e_MassH, Uncertainty on mass_H (emass_H), from Gentile Fusillo et al. (2021)
chisqH, chi square value of the fit (pure-H)(chisq_H), from Gentile Fusillo et al. (2021)

`TeffHe`, Effective temperature from fitting the dereddened G, BP, and RP absolute fluxes with pure-He model atmospheres (`teff_He`), from Gentile Fusillo et al. (2021)
`e_TeffHe`, Uncertainty of `teff_He` (`eteff_He`), from Gentile Fusillo et al. (2021)
`loggHe`, Log of surface gravity from the dereddened G, BP, and RP absolute fluxes with pure-He model atmospheres (`logg_He`) from Gentile Fusillo et al. (2021)
`e_loggHe`, Uncertainty on `logg_He` (`elogg_He`), from Gentile Fusillo et al. (2021)
`MassHe`, Stellar mass resulting from the adopted mass-radius relation and best fit parameters (`mass_He`), from Gentile Fusillo et al. (2021)
`e_MassHe`, Uncertainty on `mass_He` (`emass_He`), from Gentile Fusillo et al. (2021)
`chisqHe`, chi square value of the fit (pure-He) (`chisq_He`), from Gentile Fusillo et al. (2021)
`fuvwd`, Objects that appear to have a white dwarf in GALEX FUV-NUV
`nuvwd`, Objects that appear to have a white dwarf in GALEX NUV-Gaia Bp
`gaiawd`, Objects that appear to have a white dwarf in Gaia Bp-Rp
`wd_m_H`, Estimated white dwarf mass from fit of white dwarf with pure-H atmosphere.
`wd_m_H_e`, Estimated white dwarf mass error for pure-H atmosphere
`wd_age_H`, Estimated white dwarf age from fit of white dwarf with pure-H atmosphere.
`wd_age_H_e`, Estimated white dwarf age error for pure-H atmosphere
`wd_teff_H`, Estimated white dwarf temperature from fit of white dwarf with pure-H atmosphere.
`sec_m_H`, Estimated secondary non-degenerate from fit of white dwarf with pure-H atmosphere. If no evidence of a companion from the photometry, we performed single WD fit and report 0 for this value.
`sec_m_H_e`, Estimated secondary non-degenerate mass error pure-H white dwarf atmosphere.
`chi_sq_H`, The resulting chi squared value for the fit for hydrogen atmospheres.
`goodness_H`, The probability that the estimated masses are a good fit for the data for hydrogen atmospheres.
`wd_m_He`, Estimated white dwarf mass from fit of white dwarf with pure-He atmosphere.
`wd_m_He_e`, Estimated white dwarf mass error for pure-He atmosphere
`wd_age_He`, Estimated white dwarf age from fit of white dwarf with pure-He atmosphere.
`wd_age_He_e`, Estimated white dwarf age error for pure-He atmosphere
`wd_teff_He`, Estimated white dwarf temperature from fit of white dwarf with pure-He atmosphere.
`sec_m_He`, Estimated secondary non-degenerate star from fit of white dwarf with pure-He atmosphere. If no evidence of a companion from the photometry, we performed single WD fit and report 0 for this value.
`sec_m_He_e`, Estimated secondary non-degenerate mass error white dwarf pure-He atmosphere.
`chi_sq_He`, The resulting chi squared value for the fit for helium atmospheres.
`goodness_He`, The probability that the estimated masses are a good fit for the data for helium atmospheres.